

Numerical Maximum Lift Predictions of a Realistic Commercial Aircraft in Landing Configuration

Niko F. Bier¹ and David Rohlmann² and Ralf Rudnik³
German Aerospace Center (DLR), D-38108 Braunschweig, Germany

Within task three “Numerical Simulations” in the project “HINVA - High Lift Inflight Validation” extensive numerical verification studies based on a CAD model of DLR’s A320-232 “Advanced Technology Research Aircraft” in landing configuration are carried out. Therein special attention is paid to the effect of certain geometric features of the high-lift system, such as slat tracks, de-icing pipe etc. Also the empennage and a model of both the operational engine and a through flow nacelle are included in the geometry. The numerical simulations are carried out using two different sets of flow solver settings. The first based on the Spallart-Allmaras turbulence model represents DLR’s current best-practice. The second set follows a high-precision approach based on a differential Reynolds stress turbulence model. In this paper the structure of the task is presented along with results of initial numerical simulations assessing the influence of the slat tracks, the de-icing pipe and the TFN in comparison to the operational engine.

Nomenclature

α	=	angle of attack
<i>ATRA</i>	=	Advanced Technology Research Aircraft
<i>cf_x</i>	=	<i>X</i> component of the friction coefficient
C_L	=	lift coefficient
<i>C²A²S²E</i>	=	Center of Computer Applications in Aerospace Science and Engineering
<i>CSM</i>	=	Computational Structural Mechanics
<i>DES</i>	=	Detached Eddy Simulation
<i>DLR</i>	=	Deutsches Zentrum für Luft- und Raumfahrt (<i>German Aerospace Center</i>)
<i>ETW</i>	=	European Transonic Windtunnel
<i>FSI</i>	=	fluid structure interaction
<i>FTF</i>	=	flap-track fairings
<i>HINVA</i>	=	<u>H</u> igh Lift <u>I</u> nflight <u>V</u> alidation
<i>HTP</i>	=	horizontal tailplane
<i>IAE</i>	=	International Aero Engines
<i>IAG</i>	=	Institute of Aerodynamics and Gas Dynamics
<i>ISM</i>	=	Institute of Fluid Mechanics
<i>lcts</i>	=	lift counts (1 lct = 0.01)
<i>Ma</i>	=	Mach number
<i>max</i>	=	index indicating maximum values
<i>RANS</i>	=	Reynolds-averaged Navier-Stokes
<i>Re</i>	=	Reynolds number
<i>TC</i>	=	test case
<i>TFN</i>	=	through-flow nacelle

¹ Research Scientist, Institute of Aerodynamics and Flow Technology, niko.schade@dlr.de.

² Research Scientist, Institute of Aerodynamics and Flow Technology, david.rohlmann@dlr.de.

³ Head of Transport Aircraft branch, Institute of Aerodynamics and Flow Technology, ralf.rudnik@dlr.de.

I. Introduction

THREE-element high-lift systems consisting of slats, main wing and Fowler-type of flaps are well-established as an efficient compromise between a desired gain in lift and complexity of the mechanical system¹. In principle the aerodynamic interactions between the three elements are understood². However, because of the highly complex geometry of realistic high-lift systems and the disturbance of the principal mechanisms by vortex-dominated and detached flows at high angles of attack the CFD-based prediction of high-lift performance remains a challenging task. During the last years these capabilities have improved continuously³. And although a good agreement between CFD-predictions and wind tunnel measurements has been achieved in general, the prediction of stall mechanisms, increments in lift due to changes in geometry and flight conditions and the prediction of absolute values of maximum lift and the associated angle of attack still remains a challenging task. This is especially the case for realistic flight Reynolds numbers. Following experiences shared by the industry, the offset between high lift performance measured in real flight compared to predictions based on wind tunnel measurements or CFD simulations is still not as precise as it should be.

Against this background, the project “HINVA - High Lift Inflight Validation”⁴ aims at narrowing the gap between predictions and measured high-lift performance of future civil transport aircrafts to the accuracy which is desired from the aerodynamics design point of view. This does not only apply to the maximum lift itself but also to the corresponding angle of attack.

In its four work packages WP 1 “ATRA Flight Tests”, WP 2 “ETW Windtunnel Experiments”, WP 3 “Numerical Simulations” and WP 4 “Simulation Strategy”, HINVA aims not only at identifying the key drivers responsible for deviations in maximum lift predictions, but especially at quantifying their impact on maximum lift and its associated angle of attack. The results will be evaluated in WP 4 with the main emphasize on defining a future simulation-strategy suitable to precisely predict high-lift performance in an efficient, robust and industrial relevant way. Although special attention lies on the landing configuration, the clean configuration’s behavior will be investigated as well.



Figure 1. DLR’s A320-232 Advanced Technology Research Aircraft “ATRA”

In HINVA DLR’s “Advanced Technology Research Aircraft” (ATRA) (Figure 1), an Airbus A320-232 equipped with two International Aero Engines IAE V2527-A5 engines, is used for stall flight tests. In addition a halfmodel for cryogenic wind tunnel tests will be build and equipped with roughly 450 pressure ports covering not only the positions of the pressure ports used on the real aircraft during the flight tests, but also five spanwise cuts on all three elements and three cuts on the nacelle. A detailed CAD geometry of the ATRA is also available for CFD simulations. This offers the unique possibility to directly compare the results of all three methods for $C_{L,max}$ determination in terms of maximum lift and the associated angle of attack. Furthermore the flow topology and the pressure distributions can be compared at the exactly the same positions on all elements of the high lift wing.

Because of HINVA’s challenging objectives extensive numerical verification studies are carried out in order to analyze the influence of the geometrical modeling, the influence of the grid and the influence of numerical settings and turbulence models on numerical maximum lift prediction.

Based on a baseline geometry in landing configuration including all details that may influence stall onset, like e.g. slat-tracks, flap-track fairings, nacelle, pylon, nacelle strakes and the pre-trimmed horizontal tailplane (HTP), investigations on geometrical modeling will not only deal with the influence of the macroscopic features, e.g. trimmed, untrimmed or discarded HTP, but as well with supposedly important effects of smaller geometrical

features such as e.g. the slat-tracks, the de-icing pipe and the slat-horn, which are used to be neglected in CFD simulations for simplicity reasons. The complexity of the simulations using the baseline configuration will be stepwise increased starting from unpowered simulations in jig-shape and coupled simulations with fluid-structure interaction (FSI) up to maneuver simulations taking into account the effects of the static aerolastic deformation, engine thrust and the varying altitude during the stall maneuver.

In the first part this paper will give a detailed overview over the geometric representation of the ATRA and the associated grids. In the second part of the paper the numerical studies which will be carried out by the participating partners in work package WP 3 “Numerical Simulations” are presented. In the final part first CFD results will be presented.

II. Geometry, Computational Grids and Numerical Tools

Before presenting the six tasks of WP 3 in more detail in section III of this paper, the primary CAD model, the grid philosophy and the tools used for the numerical prediction of maximum lift are discussed in the following sections.

A. Geometry Representation

The CAD-model used in HINVA is a precise representation of the ATRA in landing configuration with fully deployed slats and flaps, a deployed aileron, the horizontal and vertical tail planes and the operational IAE V2500 engine with nacelle strake. The model is further equipped with flap track fairings and pylon end fairings, slat tracks, the slat horn and the de-icing pipe.

The designed twist distribution for the flight case is already taken into account in the geometry representation of all three elements of the high lift wing (“Flight twist”), whereas no additional bending is modeled (“Jig Bending”). Also the engine is positioned in a representative position. Different models for the ATRA in “Flight twist – Flight bending” shape as



Figure 2. Slat Track Cavities

well as in “Jig twist – Jig bending” shape exist. The latter one will be used for the coupled FSI simulations within task 3.5.

For CAD preparation the commercial software packages CATIA V5, Release 18⁵, and CADfix⁶ were used.

1. Slat Cove Elements

Since it is known from other investigations⁷ that a significant influence of the slat tracks on the pressure distribution on the suction side of the main wing may exist, only simplifications inevitable in order to generate a mesh were applied to the representation of the slat tracks in the CAD model. Mostly this applies to the intersections of the tracks with the main wing and the slat itself. In Figure 2 one can see that in reality the cavities in the wing D-nose are slightly larger in size than the tracks and although the effect of those cavities on maximum lift might not be disregarded in all cases, especially when they are not properly sealed, they were not included in the main CAD geometry. However, it is considered to assess their influence on maximum lift for some selected cases in a later part of the project. The same considerations apply to the de-icing pipe which is also represented without the cavities in the slat cove and the wing’s D-nose.

Another minor simplification is applied concerning the sealing plates close to the slat cove (Figure 3). Since these plates are in close vicinity of the slat cove in an area of supposedly detached flow, this simplification seems acceptable.



Figure 3. Real and discretized geometry of the slat tracks and the de-icing pipe in the ATRA-model

2. Flap related modifications

Further minor simplifications in the geometric representation of the ATRA were made at the flap track fairings (FTF) where the details of the kinematic itself have not been modeled and the flap is kind of free-flying since the shape of the fairing is assumed to have a significantly larger impact as the additional disturbance of the kinematic elements themselves (Figure 4).

At the flap-fuselage intersection the CAD geometry differs slightly from the real geometry: at the real aircraft the gap between flap and fuselage grows constantly in chordwise direction and is closed by a rubber sealing at the inboard side of the inboard flap. Since meshing of such small gaps is difficult applying hybrid meshes with prismatic elements to resolve boundary layers, the gap was slightly increased to allow prismatic layers to grow on both sides. Following the investigations of Keller⁸ this simplification is not expected to have any notable impact on the overall solution but leads in this case to an important increase of grid quality.

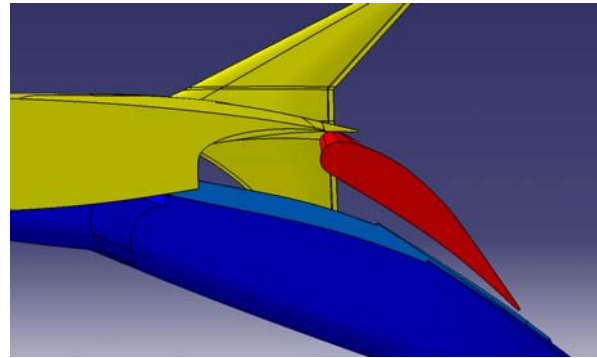


Figure 4. CAD representation of the outboard flap and the flap track fairings

3. Empennage

For the integration of the HTP into the CAD geometry a high incidence which is supposed to lead to a nearly trimmed state at maximum lift is chosen and kept throughout the whole simulations. The elevator deflection will not be altered from its neutral position at this stage. Later simulations however will also incorporate a lesser incidence angle of the HTP accordingly to a pre-trimmed state during the flight tests and in a second step within the maneuver simulations in task 3.6 it is planned to account for the elevator deflection as well, depending on the actual flight test procedure.

4. Engine

Another important driver of maximum lift and a possible cause for deviations in maximum lift predictions by flight tests, wind tunnel tests or CFD simulations might be the engine thrust which not only contributes partly to the lift but also can interact with the complex aerodynamics of the high-lift system, especially the fully deployed flaps.

The wind tunnel model however is equipped with a through-flow nacelle (TFN) which not only lacks thrust but also shows a differing geometry because of an intake modification and an increased nozzle area usually applied to TFN wind tunnel models.

Furthermore many A320 aircraft in service are equipped with CFM International CFM 56 engines which differ significantly not only in terms of size from the IAE V2500: while the IAE V2500 design favors an internal mixing of jet and bypass flow inside the nozzle, the CFM 56 is built using a more “conventional” civil turbofan design with separated jet and bypass flow.

A comparison of the three engines is given in Figure 5.

In order to assess the influence of the engine thrust the baseline CAD model is equipped with the operational IAE V2500 engine with nacelle strake. Modified CAD models are equipped with both the wind tunnel model's TFN with increased exhaust area and intake modification and the operational CFM 56 engines, respectively. A numerical simulation then offers the possibility to directly compare the results and quantify the impacts of thrust and geometry on maximum lift and the associated angle of attack.

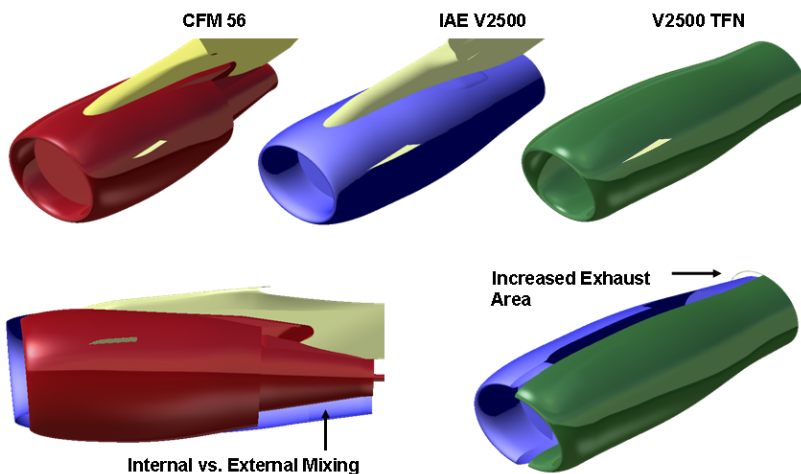


Figure 5. Comparison of CFM 56 operational engine, IAE V2500 operational engine and V2500 TFN model

5. Other features

In addition to the CAD model's level of detail other small geometric features of the so called "Lift-Improvement Package" (LIP) may have an important influence on maximum lift of the ATRA in landing configuration like e.g. a second outboard nacelle strake or an enlarged slat horn and the corresponding modification of belly fairing (see Figure 6). While it is still under discussion whether

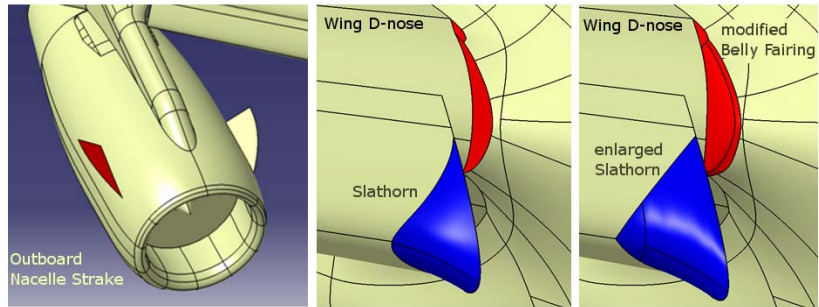


Figure 6. Lift Enhancing Features

it will be possible or not to equip the ATRA with at least some of these features during flight tests and measure the influence on maximum lift, wind tunnel and numerical simulations in fact will investigate the influence.

B. Grid generation

1. Baseline Grids

The baseline grid for the configuration with maximum geometrical detail was created using the commercial grid generator CENTAUR⁹. By the placement of different sources and the use of anisotropic stretching the grid resolution of the surface as well as in the grid domain has been adjusted aiming to achieve a high spatial resolution with as few grid nodes as possible. For the placement of the volume sources the same strategy as in former investigations³ was applied, starting with the most complex geometry. Then all test cases with less geometric details were meshed using the same sources. Since a complete modular approach as suggested by Acheson and Kornegay¹⁰ for all geometric details to be investigated seems desirable but nonetheless unfeasible, this approach supposedly leads to comparable grids for all configurations and assumable minimizes grid influences in the simulations.

For the surface resolution an anisotropic stretching in spanwise direction of two was applied for the wing parts

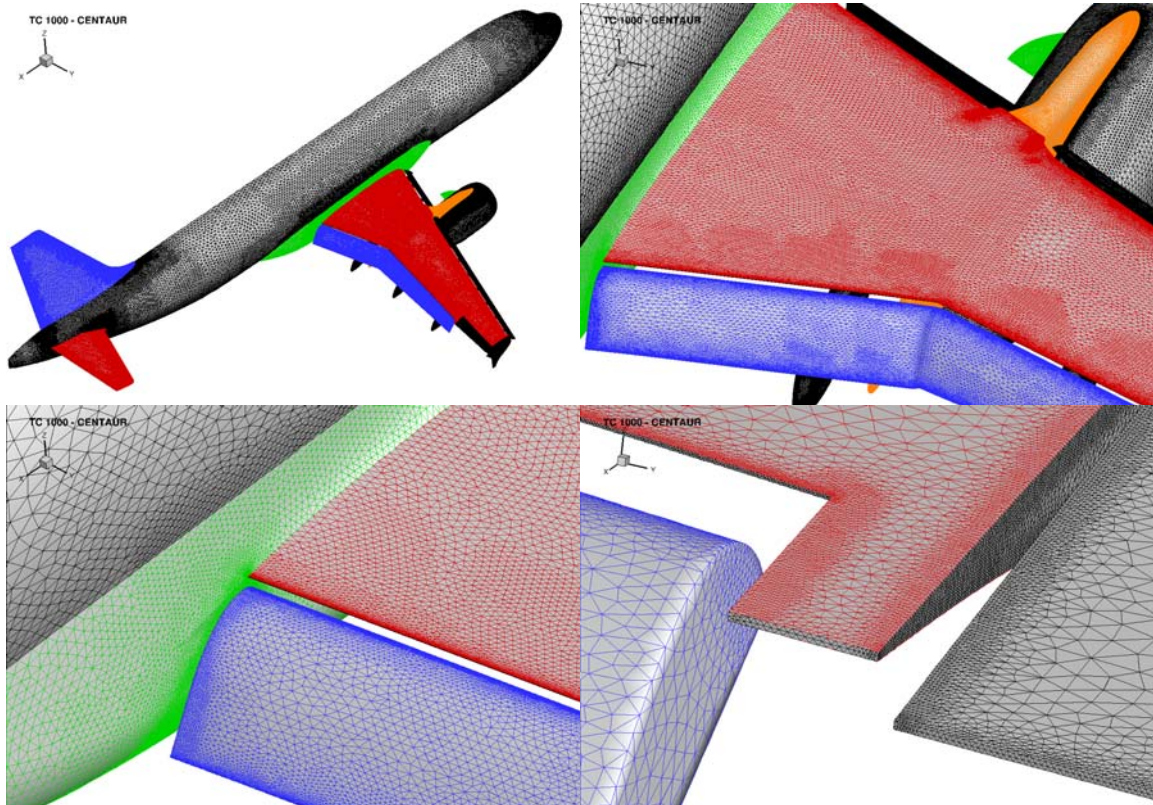


Figure 7. Final surface grid of the ATRA in landing configuration (baseline grid)

outboard of the engine to reduce the overall number of points. In the inboard wing section the anisotropic stretching was reduced to unity since the complex flow physics and possible interactions between various vertical flow systems (horseshoe vortex, slat horn vortex, nacelle strake vortex, etc.) with the boundary layers may well show significant changes in spanwise direction. All trailing edges were modeled as blunt trailing edges and resolved with at least two cells to decouple the pressure and the suction side in the dual grid metric of the TAU Code. In most cases the trailing edges could be meshed with structured hexahedrons, again in order to reduce the overall number of points.

In order to resolve the vortices arising from e.g. the slat horn or the nacelle strake, the initial source placement was adapted based on preliminary simulations for different angles of attack between 7° and α_{\max} . Figure 7 shows the final surface grid of the baseline configuration (top left) along with a view on the inboard wing section (top right), the inboard flap-fuselage junction (bottom left) and the outboard flap-wing-aileron junction (bottom right).

To be able to use the grid of one specific configuration throughout the whole range of the flight test campaigns' Mach and Reynolds number variations 40 layers of prismatic elements were used, having a first spacing that ensures values of $y^+ < 1$ for all cases, except for the suction peaks on the slat at high angles of attack where values of $y^+ < 3$ can be reached. To avoid chopping of the prismatic layers the surface resolution in areas with high curvature was increased (see e.g. Figure 7, bottom right). With this approach a baseline grid without any chopping could be generated for the clean configuration whereas for the different grids of the ATRA in landing configuration a minimum of not less than 30 prismatic layers was achieved in all cases.

A stretching ratio for the prismatic elements was chosen in such a way that the final height is approximately twice as high as the final boundary layer on the main wing trailing edge for the lowest Reynolds number. The outer block's farfield boundary-condition is located at a distance of 100 half spans from the aircraft. Depending on the actual geometric complexity, the final grids consist of 68 to 81 million grid points in total.

For later simulations with the Reynolds stress turbulence model the first cell height will for convergence reasons be adapted to values not larger than $y^+ = 0.4$ and the stretching ratio will be adapted correspondingly to achieve an unchanged final height of the prismatic layer.

2. Variations in the Discretization

Because of the realistic geometric representation the numbers of points in the hybrid structured/unstructured baseline grids are already very high and therefore it would be very difficult to perform a grid refinement study with the given computational resources. However, an assessment of the baseline grids quality with respect to the capability to predict maximum lift and stall behavior of the ATRA is strongly desired. Therefore two additional gridding philosophies will be applied to the baseline configuration:

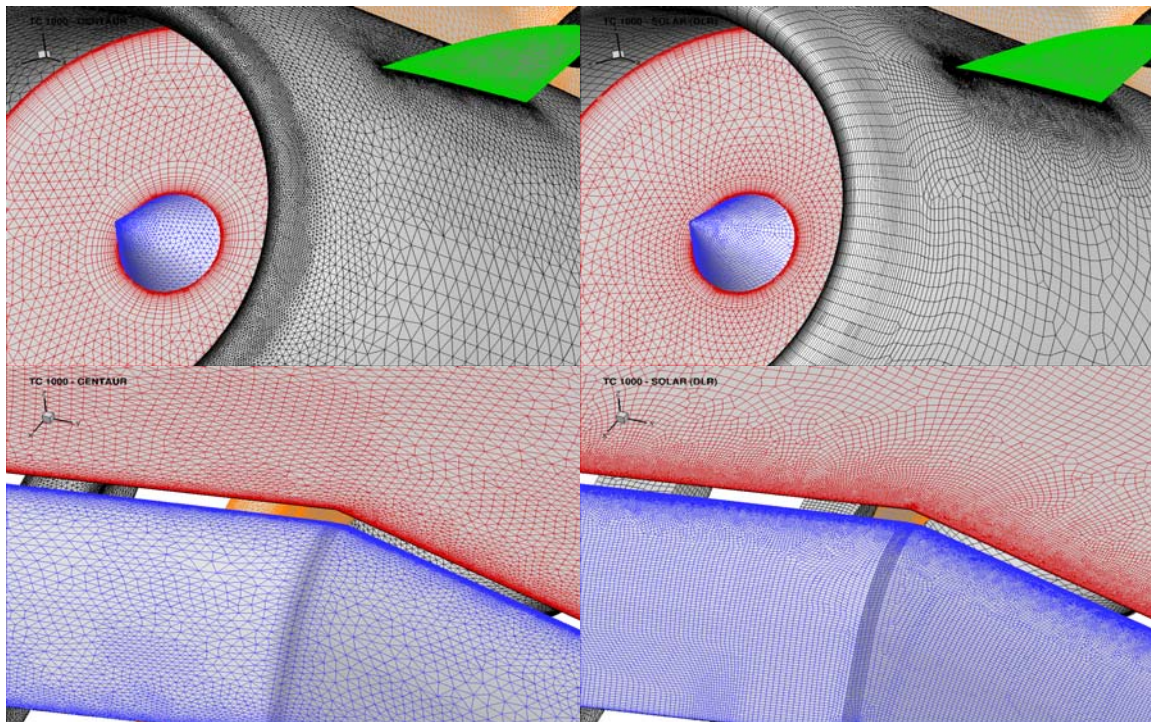


Figure 8. Comparison of baseline CENTAUR surface grid (left) and SOLAR surface grid (right)

In the first grid variation a spatial resolution comparable to the one used for maximum lift simulations in EUROLIFT II³ with approximately 40 million points in total will be applied. It is assumed that this grid will be able to show in the first place the influence of a coarser discretization of areas with high curvature like e.g. the leading edges of the slats, the wing and the flaps.

In the second variation special attention will be laid on the resolution of wakes and the jet, especially on a low stretching ratio of the tetrahedral elements since there is reason to believe that a higher stretching ratio in the vicinity of the wing may well lead to wrong predictions of separations. In addition the stretching ratio of the prismatic elements perpendicular to the surface will be increased to achieve a significantly thicker region of prismatic layer elements and assumable to better conserve the preceding elements' wakes – even if therefore the quality of the intersection of prismatic and tetrahedral elements will be worse.

3. SOLAR grids

In addition to the baseline CENTAUR grids partners from the Center of Computer Applications in Aerospace Science and Engineering (C²A²S²E) have generated a grid with the mesh generator tools of the SOLAR CFD¹¹ system. Its quadrilateral dominant surface grids and the corresponding hexahedral dominant layers near the surfaces offer a high potential for high lift applications by aligning the surface and volume elements with the main direction of the flow.

To keep the SOLAR grid similar to the baseline grids only limited use of anisotropic stretching was made. The first cell height was chosen to be the same as for the CENTAUR grids, but as SOLAR builds hexahedral layers with a constant stretching ratio until a cell aspect ratio of unity in the outer layer is reached the structured parts of the grids a merely comparable. However, a similar overall number of points was achieved for both corresponding grids.

Figure 8 shows a comparison of the baseline grid generated with CENTAUR (left side) and the corresponding SOLAR grid (right side) for the nacelle intake (top) and the kink region on main wing and flap (bottom).

Especially in regions with high curvature, like e.g. the intake, the quadrilaterals allow both a better alignment of the elements on the surface perpendicular to the flow and, with a given number of points, a better resolution of the flow in streamwise direction.

Furthermore a higher stretching at the surface results in more even hexahedrons at the outer layer and thus, in a better junction to unstructured tetrahedral elements in the field.

Figure 9 shows exemplarily the differences in the volume grids for TC 1000 for two cuts in the outer wing section in streamwise direction (top and middle) and perpendicular to the flow (bottom). The grid generated with CENTAUR is shown on the left side (black) and the grid generated with SOLAR (blue) on the right side. One can see the dependency between the surface resolution and the structured layers for SOLAR grids, especially at the wing trailing edge and the flap nose, respectively the weak dependence for the CENTAUR grid in the upper and middle part of Figure 9. The lower part shows the wing body junction near the wing trailing edge: here the coupling between surface resolution and structured layer leads for the SOLAR grid to an even poorer resolution of the corner flow compared to the CENTAUR grid which may have significant impacts on the overall flow prediction¹².

Since this is to the knowledge of the authors the first time a SOLAR grid of a realistic high lift configuration was successfully built and simulated using the TAU Code no best practice gridding guidelines exist yet. An assessment of the results and a comparison to the results achieved with the corresponding CENTAUR grids will therefore be done in work package WP 4. Special attention will be paid on the influence of the SOLAR-inherent junction between surface resolution and overall height of the structured layers off the walls.

4. GRIDGEN grids

Amongst others to overcome the limitations of both CENTAUR and SOLAR for the studies wing-HTP interference effects partners from the Technische Universität Braunschweig's Institute of Fluid Mechanics (ISM) and the Universität Stuttgart's Institute of Aerodynamics and Gas Dynamics (IAG) will generate GRIDGEN¹³ meshes for a simplified clean configuration (IAG) and the aft part of the landing configuration (ISM). The approach will be presented along with the structure of the task 3.3 in section III C of this paper.

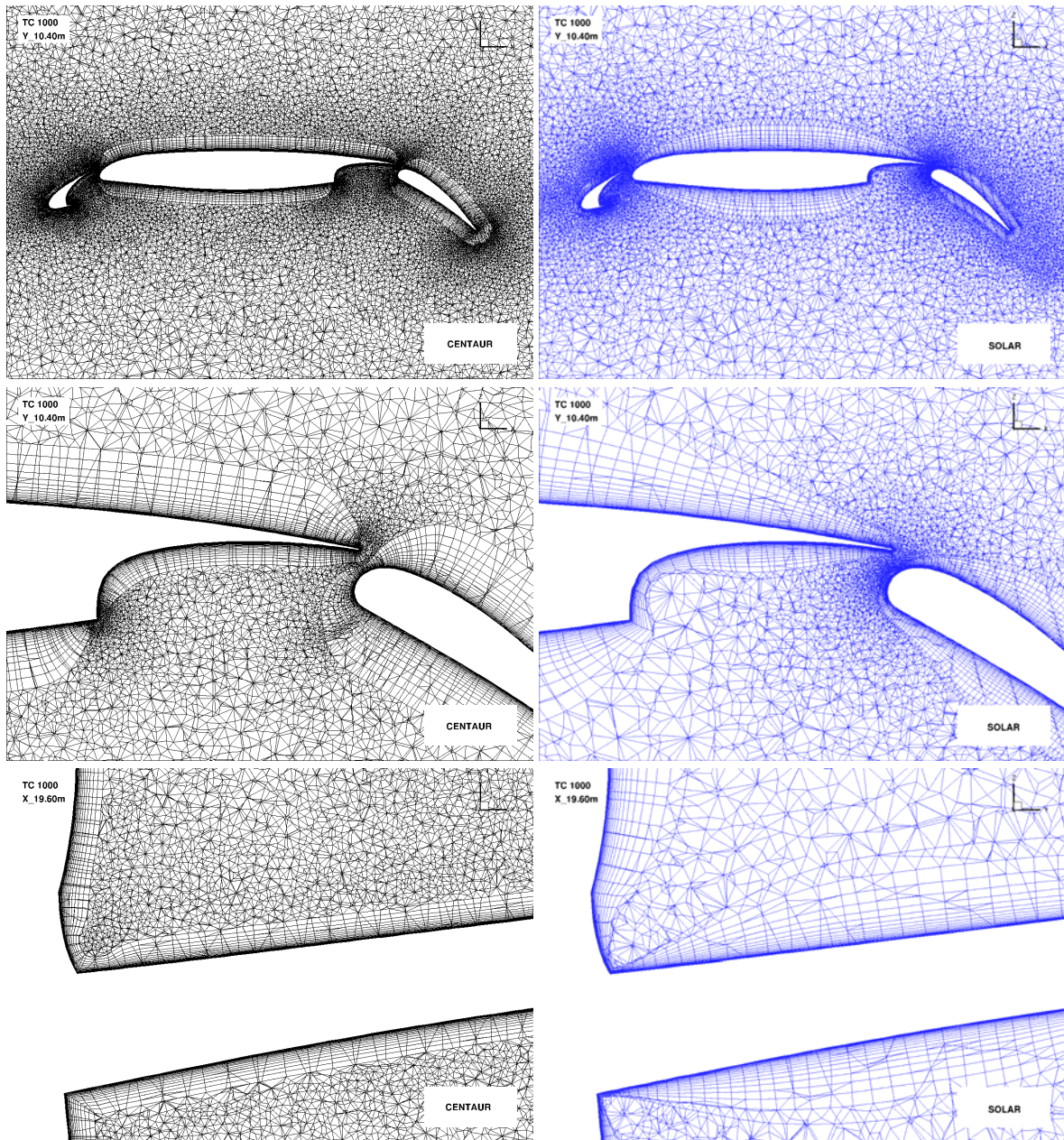


Figure 9. Comparison of baseline CENTAUR volume grid (left) and SOLAR volume grid (right)

C. Numerical Tools

1. The DLR TAU Code

The TAU Code^{14,15} is a Navier-Stokes solver for the simulation of viscous and inviscid flows around general complex geometries. The solver is based on the finite volume method and uses a dual-grid approach, where the flow variables are associated with the vertices of the original grid. The solver can handle different cell types and can be used on structured and unstructured (hybrid) grids. Generally, a semi-structured grid layer above surfaces is used to resolve boundary layers, whereas the rest of the computational domain is filled with an unstructured grid. The solver computes the fluxes with a second-order central scheme or one of various upwind schemes with linear

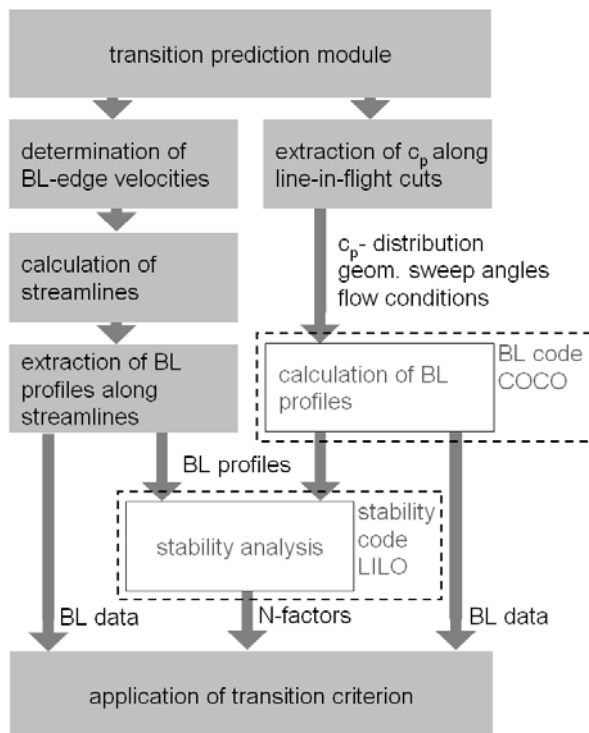


Figure 10. Transition Prediction Module

turbulence model¹⁹ (SSG/LLR- ω), will be applied because of its potential rather to resolve than to model the vortical flow systems which dominate both maximum lift and the stall behavior of the ATRA

In both approaches a Jameson-type scalar dissipation with scaling coefficients $k_2 = 1/2$ and $k_4 = 1/64$ was chosen for the first 5.000 iterations of every initial angle of attack of each test case. Then a matrix dissipation scheme was applied until a converged state was reached. For time integration the implicit backward Euler LUSGS scheme was applied. With respect to convergence behavior a three level multigrid acceleration was used when possible.

2. Transition Prediction

For automatic transition prediction in Navier-Stokes computations, a coupled program system was developed, consisting of a transition prediction module²⁰ implemented directly into the unstructured/hybrid Navier-Stokes solver TAU. Specific elements of the module are the laminar boundary-layer code COCO²¹ for swept, tapered wings and the linear stability equations solver LILO²². The transition prediction module, which has been developed with special focus on predicting transition for flows around general, complex, three-dimensional geometries, supports parallel computing.

Within the numerical simulations of HINVA the boundary layer data needed for the transition prediction is taken from the C_p -distribution along line-in-flight cuts as shown in Figure 10. As transition criteria the linear stability theory in form of the e^N -method is applied²³, treating the N-factors for Tollmien-Schlichting and crossflow instabilities independently.

Transition prediction is used in task 3.1 for the preparation of the first flight test. Based on the transition predictions for different configurations, Mach and Reynolds numbers hot film arrays will be defined which will be used to measure the transition location during flight tests. In task 3.3 transition prediction is used in the numerical simulations for selected test cases both to assess the influence of transition on the simulation results and to further increase the automatic transition prediction capabilities of DLR for industrial relevant commercial aircraft configurations.

reconstruction for second-order accuracy. Time integration is performed by either applying an explicit, multistage Runge-Kutta scheme or an implicit, lower-upper symmetric Gauss-Seidel (LU-SGS) scheme. Turbulent flows are modeled using different Spalart-Allmaras, $k-\omega$ models, or Reynolds stress turbulence models (RSM). For transitional flows, laminar regions can be designated by the definition of polygon lines on the surface of the geometry and prescribing the maximum height of the laminar region over the surface. For these computations, the turbulent production terms are suppressed in the laminar flow area. For convergence acceleration residual smoothing, local time stepping and a multigrid approach can be applied. To extend the solver capability to incompressible flows, a low-Mach-number preconditioning approach is implemented.

Based on experience at DLR as well as on results from the first AIAA Highlift prediction workshop^{16,17} two approaches will be applied for the numerical simulations in HINVA: The first approach features the Spallart Allmaras¹⁸ turbulence model with robust numerical settings accordingly to current DLR best practice. In the second approach more sophisticated settings and the highest-fidelity physical model available in the TAU Code, a differential RSM

III. Numerical Simulations in HINVA

For the German Aerospace Center HINVA offers for the first time the chance to validate maximum lift predictions for realistic high-lift civil transport aircraft configurations based on wind tunnel measurements and CFD simulations with actual flight test data. As described by Rudnik⁴, within this framework the numerical simulations not only serve as a means for maximum lift prediction but also provide suggestions for the placement of measurement techniques on the aircraft and the wind tunnel model. Furthermore they provide an assessment of the measurement techniques influence on the measurements themselves as well as the possibility to validate and – if necessary – improve ETW’s wind tunnel corrections for half models in the non-linear part of the lift curve.

Numerical simulations of maximum lift under flight conditions in conjunction with the supercomputing resources available at DLR offer for the first time the possibility to conduct extensive verification studies by stepwise increasing the geometrical setup as well as the fidelity of the numerical methods ranging from fully turbulent simulations with the SA turbulence model to time-resolved maneuver simulations with operational engine, varying Mach- and Reynolds number and time resolved deformation of all three elements of the high-lift wing.

The tasks of work package WP 3 “Numerical Simulations” are shown in Figure 11 and will be presented in detail in the following paragraphs.

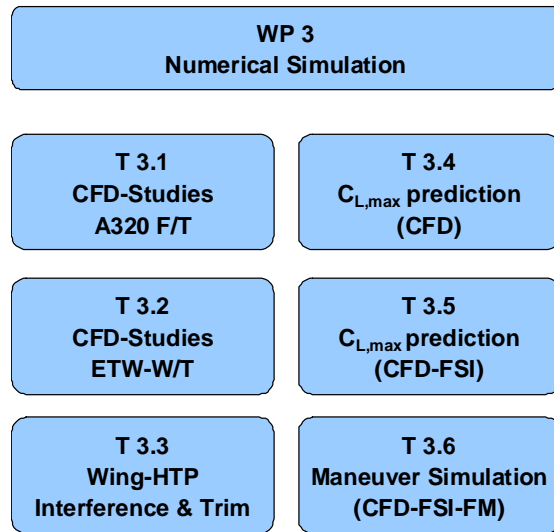


Figure 11. Structure of work package WP 3 “Numerical Simulations”

A. Task 3.1: CFD-Studies – A320 Flight Tests

The first task 3.1 “CFD Studies – A320 Flight Tests” aims to predict the stall behavior and the corresponding flow features like separations, vortices etc. of the flight test aircraft at a velocity of $Ma = 0.204$ and a Reynolds number of $Re = 16.9 \text{ e}+06$. Based on these simulations areas for the placement and resolution of measurement techniques such as pressure belts and flow cones were defined together with WP 1. Figure 12 shows exemplarily the skin friction lines and color coded the areas with negative friction coefficients in x-direction (c_{fx}) on the surface indicating possible areas of separation the non-linear part of the lift curve.

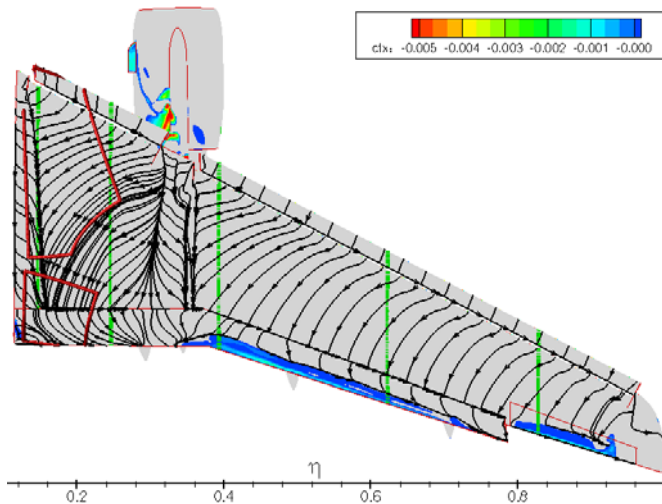


Figure 12. Placement of Measurement Techniques Based on Preliminary CFD studies

Based on the simulations pressure belts were defined at the five spanwise positions marked with green lines, each equipped with roughly 75 pressure tabs distributed on all three elements. In addition unsteady pressure sensors were defined in the belts at locations of special interest. Based on additional numerical simulations covering the whole range of flight test conditions the placements were adapted and the sensitivity of the differential sensors was defined in a way that allows the finest resolution without risking to overcharge and to damage the sensors. Future work in task 3.1 will deal with the numerical analysis of the effect of the pressure belts on the flow itself by including them into the CAD model of the flight test aircraft as shown in Figure 14.

The numerical simulations and the underlying CAD model also served as a means to define areas of interest for optical measurement of flow

topology by applying flow cones to the wing and adjusting the observation area of flow visualization cameras inside the fuselage (red marked areas). This allows the measurement of the direction of the flow near the surface and the detection of separations which provides only qualitative but in return two-dimensional data to validate the numerical predictions.

Transition is another possible important driver of the accuracy of maximum lift predictions, since in most cases the roughness and the surface representation of the high lift wing differ between a CAD model, a wind tunnel model and the real aircraft.

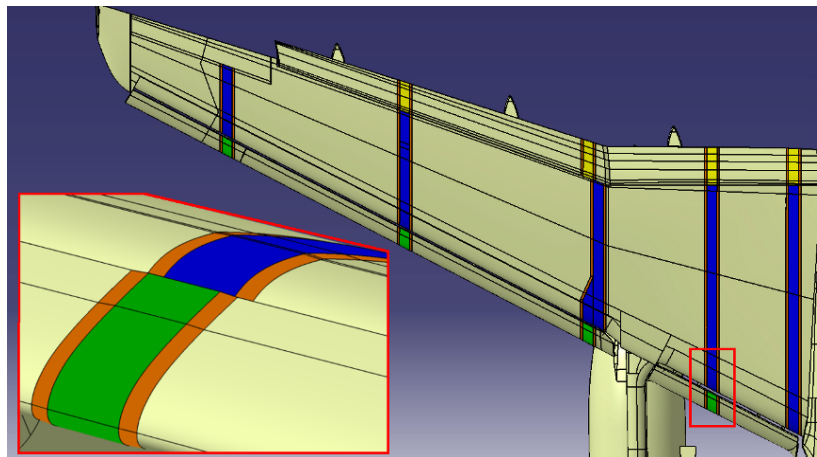


Figure 13. CAD Model of the Pressure Belts

Furthermore automatic transition prediction for industrial relevant high lift configurations is still a challenging task, although progress has been made recently²³, and there is only limited validation data for high lift wings from flight tests, e.g. published data from flight tests with an Airbus A310²⁴, available to DLR.

In order to assess the influence of transition on the maximum lift of the configuration and to generate validation data for the numerical simulation hot film arrays will be placed in two spanwise sections on the high lift wing during the tests. Based on CFD-based transition predictions the arrays were proposed to be placed at spanwise positions of 21% inboard of the nacelle and 58% in mostly undisturbed flow, respectively. The spacing of the arrays again follows propositions based on numerical predictions in order to capture not only the position of the laminar-turbulent transition up-

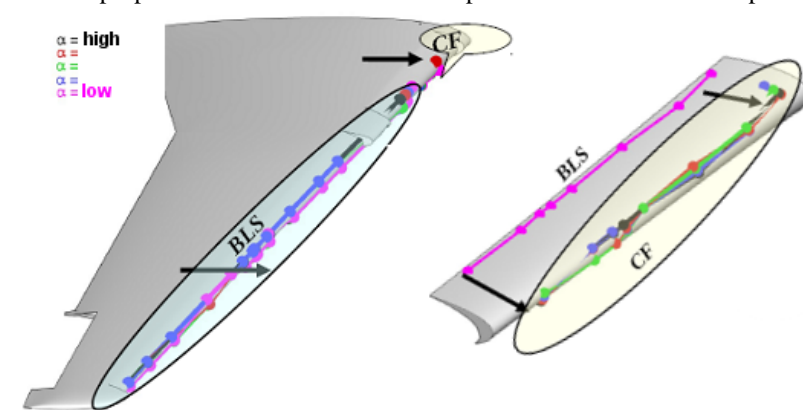


Figure 14. Example of predicted transition locations on the inboard slat and the wing at a Mach number of $Ma = 0.20$

and downstream of the stagnation point but the position of the stagnation point itself as well.

Figure 14 shows exemplarily the results of the automatic transition prediction for the main wing and the inboard slat at a Mach number of $Ma = 0.20$. While on the inboard slat and the inboard section of the wing transition is predicted due to crossflow already for moderate angles of attack, on the outer part of the wing transition is set where a laminar separation is predicted by the transition prediction module.

For a second flight test campaign measurements of the velocity magnitude and direction in- and outside the boundary layer is planned. For the design of closed and adjustable boundary layer probes²⁵ which are being built also the results from the numerical simulations were taken as a aerodynamic design basis as well as a basis to design the application of the probe onto the wing surface. Later on numerical simulations will also serve as a basis to decide where to apply the probes during flight tests.

B. Task 3.2: CFD-Studies – ETW Wind Tunnel Tests

The focus of the numerical simulations in task 3.2 is twofold: in a first step coupled FSI simulations help to design a pre-deformed high lift wing that is supposed to preserve geometrical similarity to the high lift wing, i.e. twist and bending distribution, for representative flight test conditions near maximum lift. These representative conditions will be defined based on deformation measurements during the flight tests. Figure 16 shows the design process to achieve this goal, assuming that DLR's FSI capabilities are sufficiently accurate:

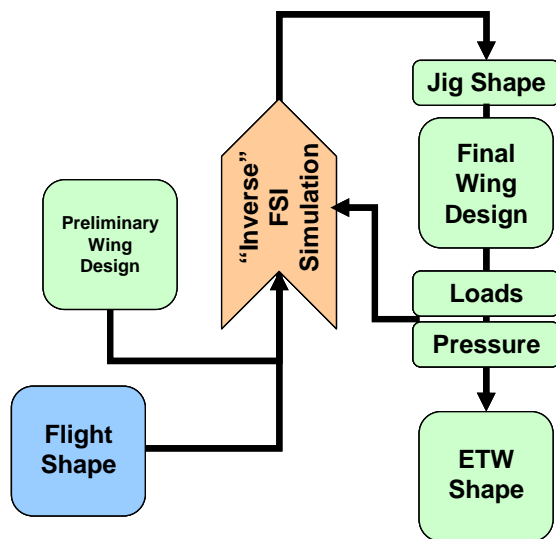


Figure 15. Design process for a pre-deformed wind tunnel model

- 1) Based twist and bending measurements of all three elements of the high lift wing during the flight tests a representative geometry for maximum lift will be defined together with work package WP 1 “Flight Tests”.
- 2) With a preliminary structural model of the wind tunnel model which is achieved from a preliminary design study and the wind tunnel conditions at the design point an inverse FSI simulation leads to the final jig shape of the model.
- 3) Based on the simulated jig shape a final design will take place.
- 4) A numerical verification of the final ETW shape with the resulting structural model concludes the design process or – if necessary – allows for a new simulation of the model jig shape in an iterative design process.

The second part of task 3.2 deals with the numerical assessment of the influences on maximum lift prediction associated with the half model technique. Since it is known from other investigations^{26,27} that both the wind tunnel walls as well as the peniche that keeps the model outside the wall’s boundary layer (see Figure 15) may have an influence on the achievable maximum lift, numerical simulations will investigate their influence. In order to separate the effects the simulations will be carried out with stepwise increased complexity ranging from simulations with

- 1) only the wind tunnel model under wind tunnel onflow conditions,
- 2) the model with peniche mounted on a flat plate representing the wall of wind tunnel and
- 3) the model with peniche and the surrounding wind tunnel.

C. Task 3.3: Wing-HTP-Interference and Trim

One major difference between today’s maximum lift predictions using CFD or wind tunnel measurements and the corresponding flight tests is the empennage, and in particular the horizontal tail plane, which is usually not part of high lift models. Within task 3.3 mainly the partners from ISM and IAG will investigate the effect of the empennage and wing-HTP interference effects on the predicted maximum lift. In both cases special attention is paid both to a refined resolution of the wing wake and to a sufficient resolution of the fuselage’s boundary layer which may at the location of the HTP be significantly thicker than the corresponding one of a flat plate because of the contraction of the fuselage.

The main focuses of IAG are investigations of the tail plane flow with regard to interference effects with the flow on the main wing, the HTP trim angle and unsteady loads both in cases with attached and separated flow on the main wing. Since the investigations besides time resolved uRANS feature Detached Eddy Simulations (DES) with an increased resolution of the grid compared to RANS simulations they will be conducted with the clean configuration for which also maximum lift flight tests will be performed. For the final DES a simplified geometry



Figure 16. A320 wind tunnel model in ETW

without flap track fairings will be meshed using C-type grids around wing and HTP and blocks of structured hexahedrons in the wake of the wing. The grids will be built with GRIDGEN¹³ based on a baseline CENTAUR grid in a stepwise approach and the influences of the grid as well as the influences of the geometrical simplifications will be investigated.

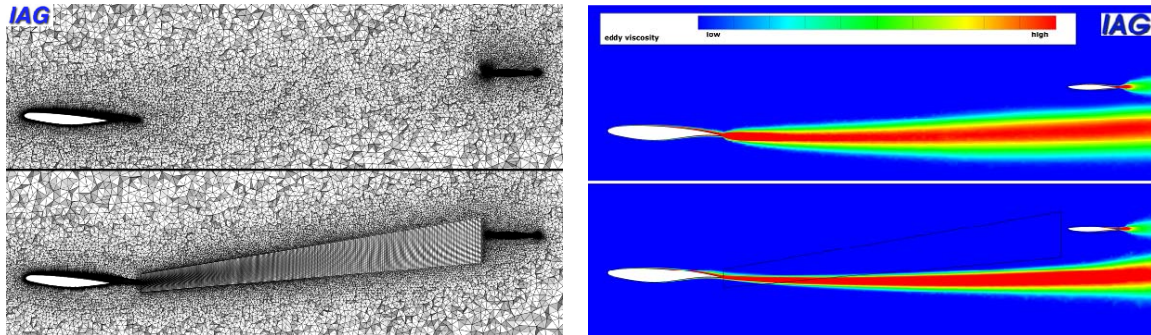


Figure 17. Increased wake resolution and eddy viscosity distribution for the clean configuration

Based on a preliminary grid Figure 17 shows exemplarily on the left side the initial and the with hexahedral blocks increased spatial resolution between wing and HTP and on the right side the eddy viscosity distribution in the wake of the main wing. It can be seen that even though there is still an O-type grid around the wing the grid is less dissipative and conserves the wake significantly better than the original grid.

The work of ISM again features investigations on wing-HTP interference effects for the ATRA in landing configuration in full geometric detail. Since on one hand building C-type grids for this configuration is extremely difficult and a high resolution of the wake is mandatory on the other hand the overset grid chimera-approach²⁸ is chosen for the investigations: The front part of the configuration just behind the main wing will be discretized with an hybrid CENTAUR-grid whereas for the rear part with the empennage a C-type grid using GRIDGEN will be built. With respect to computational cost a local wake refinement together with multiple adaptation cycles is chosen over a generally increased resolution of the wing wake. Like for the clean configuration the structured parts of the GRIDGEN grid part allows a resolution of both the fuselage boundary layer and the HTP boundary layer with structured elements as depicted in Figure 18. Especially at the junction of HTP and fuselage the structured elements are supposed to better resolve the horseshoe vortex which is in conjunction with the fuselage boundary layer one of the major drivers of the HTP flow.

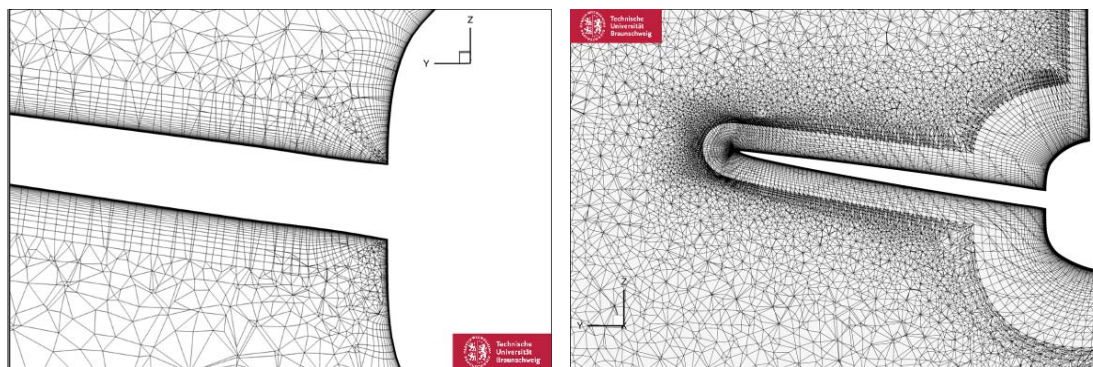


Figure 18. HTP boundary layer resolution with CENTAUR (left) and GRIDGEN (right)

D. Task 3.4: $C_{L,max}$ prediction (CFD)

Task 3.4 forms the backbone of the numerical simulations in HINVA. Work involves CAD preparation, grid generation, definition of common parameter settings for the numerical simulations, extensive numerical verification studies and numerical predictions of maximum lift. The verification studies consist of an assessment of the influence of various numerical settings, physical modeling and geometrical detail like e.g.

- 1) dissipation settings and low Mach number preconditioning
- 2) time resolved uRANS vs. steady state RANS simulations,
- 3) pitch procedure with discrete or continuous increments of different size in angle of attack,
- 4) transition due to crossflow or Tollmien-Schlichting instabilities,
- 5) possible hysteresis effects,
- 6) flap-engine interactions for operational engine and TFN,
- 7) empennage and trim settings,
- 8) small geometrical features like e.g. outboard nacelle strake and enlarged slat horn.

Later on comprehensive validation studies will compare the numerical results with results from wind tunnel experiments and flight tests, identify possible reasons for deviations and assess as far as it will be possible the quantifiable influence on maximum lift.

In addition during the flight tests the influence of variations in flight conditions on maximum lift such as flight level, weight and variations in the position of the center of gravity will be investigated. Based on the most accurate grid for the basis setup, these influences will be simulated and compared to the measured data. This will be done not only on the basis of polar measurements and simulations, but also by measurements at stabilized points and simulations with the same angle of attack, the same lift coefficient and the same loading, i.e. the same percentage of maximum lift.

An excerpt of the test case matrix and some first results of task 3.4 are discussed in section IV of this paper, whereas the fundamental work in CAD preparation and grid generation have already been presented along with the ATRA geometry in section II.

E. Task 3.5 & 3.6: $C_{L,max}$ prediction (FSI & Maneuver)

While extensive verification studies and maximum lift predictions using CFD methods will be conducted in task 3.4, task 3.5 will extend the predictions by taking into account static aeroelastic effects. This is accomplished by coupling the flow solver TAU to the commercial finite-element structural analysis software NASTRAN²⁹ as presented by S. Keye³⁰. DLR's FSI approach (Figure 19) incorporates a direct coupling between CFD and CSM domains using interpolation routines for mapping aerodynamic loads to the structural model and transferring structural deflections back to the CFD surface mesh, and a volume mesh deformation algorithm.

The simulation starts from an initial CFD solution computed on the jig shape geometry. For each surface element in the CFD grid the interpolation module computes a force vector using static pressure and friction coefficients, cell face area and cell orientation. Then, aerodynamic forces are mapped to the structural nodes located on the coupling surface using a nearest neighbor search algorithm³¹. This procedure ensures a conservative interpolation with respect to force and moment balance on both CFD and CSM side.

Next, a linear, static structural analysis is performed and the resulting nodal deflection components along the coupling surface are mapped back to the CFD surface mesh. Because the nearest neighbor search algorithm used before is not appropriate for deformation fields, an interpolation scheme based on radial basis functions (RBF) is used³¹. The technique is particularly well suited for smooth functions, like the deformations of aerodynamic structures considered here.

Before a new flow solution is started, the interpolated surface nodal deflections are extrapolated into the volume mesh, again by using an RBF-based approach. In order to achieve a gradual decline of nodal deflections from the coupling surface into the flow field, the resulting deflections are superimposed with a weighting function based on wall distance.

Finally, a new CFD solution is computed on the deformed mesh. Iteration proceeds until user-defined convergence criteria, based on either flow or structural parameters, are accomplished.

A structural model of the ATRA with distributions of mass and stiffness for all elements of the high lift wing, the fuselage and the empennage was provided to DLR and adapted to fit the needs of the simulation chain.

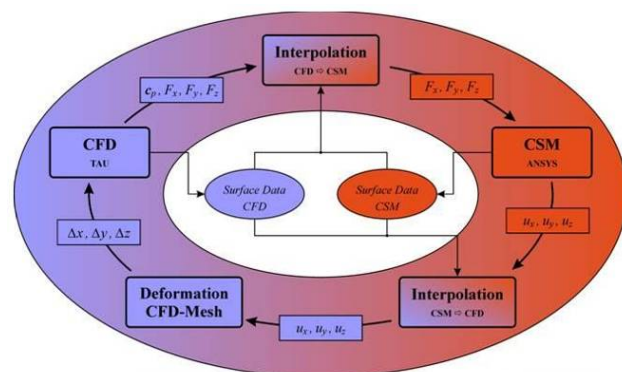


Figure 19. DLR-procedure for FSI Simulations

Maneuver simulations in task 3.6 will finally expand the FSI simulations by an additional coupling to a flight mechanics module. With this simulation environment it is planned to “re-fly” in a time-resolved uRANS approach the stall flight tests numerically, including deformation, operational engine, trim and variations of Mach- and Reynolds number. Although the time dependent changes will be prescribed during the numerical simulations this will be, at least to the knowledge of the authors, the first time such a simulation approach is used to simulate maximum lift of a commercial transport aircraft in landing configuration.

IV. Test Case Matrix and First Results

A. Test Case Matrix

Based on the factors possibly influencing maximum lift described in section III of this paper, a comprehensive matrix of more than 100 test cases (Figure 20) was defined for flight and wind tunnel tests as well as for numerical simulations, including variations in configuration, geometric details, Mach and Reynolds numbers, etc. Not included in the matrix are additional numerical cases due to variations of numerical settings like e.g. turbulence model, dissipation, RANS vs. uRANS simulations and different approaches of incrementing the angle of attack.

It is obvious that it is for practical reasons impossible to investigate the whole matrix in full amount. Therefore, based on initial CFD simulations and results from the first flight test, only the assumable most relevant test cases will be chosen and investigated.

Test Case	Configuration	LIP	Weight [t]	Ma / Re [-] / [E06]	Height [ft]	Type	Method
Basis Configuration							
TC 1000	Landing: $\delta_f = 40^\circ / \delta_s = 27^\circ$	No	70	0.204 / 16.9	8.200	Polar	F/T, CFD
TC 1001	TC1000 – no Slat Tracks	No	70	0.204 / 16.9	8.200	Polar	CFD
TC1003	TC1000 – with De-Icing Pipe	No	70	0.204 / 16.9	8.200	Polar	CFD
TC1006	TC1000 – with V2500-TFN, no Empennage	No	70	0.204 / 16.9	8.200	Polar	CFD, W/T
TC1007	TC1000 – with V2500-TFN	No	70	0.204 / 16.9	8.200	Polar	CFD
TC1008	TC1000 – with CFM-56-TFN, no Empennage	No	70	0.204 / 16.9	8.200	Polar	CFD
Basis Configuration with Deformation							
TC 1040	TC1000 (tbc.) – Twist: Flight, Bend: Flight	No	70	0.204 / 16.9	8.200	Polar	CFD
TC 1045	TC1000 (tbc.) – Twist: Flight, Bend: Flight Shape from F/T 1	No	70	0.204 / 16.9	8.200	Polar	CFD
TC 1046	TC1000 (tbc.) – Twist: Flight, Bend: Flight Shape from F/T 1 – stabilized Point	No	70	0.228 / 18.9	8.200	$C_A = \text{high}$	CFD
TC 1050	TC1000 (tbc.) – FSI	No	70	0.204 / 16.9	8.200	Polar	CFD
TC 1051	TC1000 (tbc.) – FSI – stabilized Point	No	70	0.228 / 18.9	8.200	$C_A = \text{high}$	CFD
TC 1061	TC1000 (tbc.) – SSK, prescribed motion, numerically trimmed	No	70	0.204 / 16.9	8.200	Polar	CFD
Basis Configuration – Stabilized Points							
TC 1082	Landing: $\delta_f = 40^\circ / \delta_s = 27^\circ$	No	70	0.228 / 18.9	8.200	$C_A = \text{low}_1$	F/T, CFD
TC 1083	Landing: $\delta_f = 40^\circ / \delta_s = 27^\circ$	No	70	0.263 / 21.8	8.200	$C_A = \text{low}_2$	F/T, CFD
TC 1092	Landing: $\delta_f = 40^\circ / \delta_s = 27^\circ$	Yes	70	0.222 / 17.5	9.800	$C_A = \text{low}_1$	F/T, CFD
Basis Configuration – Variations in Flightlevel							
TC 1100	Landing: $\delta_f = 40^\circ / \delta_s = 27^\circ$	No	70	0.224 / 16.0	13.100	Polar	F
TC 1200	Landing: $\delta_f = 40^\circ / \delta_s = 27^\circ$	No	70	0.257 / 15.0	19.700	Polar	F, C
Basis Configuration – Variations in Weight							
TC 1400	Landing: $\delta_f = 40^\circ / \delta_s = 27^\circ$	No	50	0.178 / 14.0	9.800	Polar	F
TC 1482	Landing: $\delta_f = 40^\circ / \delta_s = 27^\circ$	No	50	0.199 / 15.7	9.800	$C_A = \text{low}_1$	F

Figure 20. Test Case Matrix (Landing Configuration, Excerpt)

Initial polar computations with the SA turbulence model of test cases TC 1000, TC 1001, TC 1003 and TC 1007 as well as for the clean configuration have already been carried out in the first phase of HINVA prior to the flight tests in order to investigate

- 1) the influence of the slat tracks and the de-icing pipe (TC 1001 vs. TC 1000 and TC 1003),
- 2) the influence of the operational engine compared to the TFN (TC 1000 vs. TC 1007)
- 3) the influence of different increments in angle of attack

First results are presented in the following sections.

B. First results

1. Convergence Criteria and Lift Curves

All polar computations so far were started “from scratch” at a moderate angle of attack of 7.0 degrees within the linear part of the lift curve. Based on a converged solution at each angle of attack the subsequent one was simulated. The angle of attack was increased by 1.0 degree in the linear part and by 0.5 degrees in the non-linear part. For each angle of attack between 20.000 and 40.000 iterations were simulated before a converged solution was obtained. Figure 21 shows exemplarily the convergence history for TC 1000 for an angle of attack in the linear part of the lift curve and one near maximum lift.

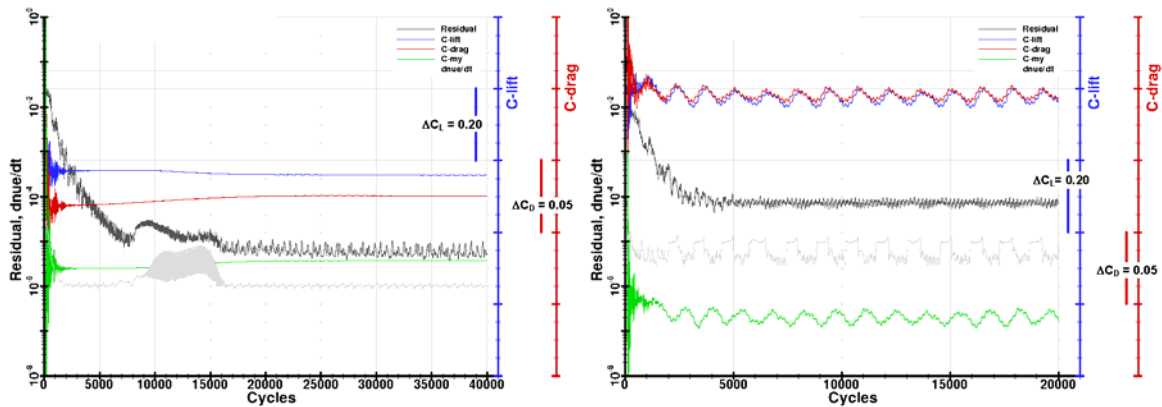


Figure 21. Convergence history for TC 1000 at medium (left) and high (right) angle of attack

It is important to notice that especially for the medium angle of attack not only before 7.500 cycles the beginning separation at the wing tip can be noticed in the force coefficients as well as in density and turbulence residuals. A converged solution is obtained after 25.000 cycles. However, for the high angle of attack already after 7.500 cycles the solution is converged with fluctuations in lift within ± 0.03 from the steady mean value. For even higher angles of attack the magnitude increases some but for pre-stall conditions a steady mean value was always obtained.

Figure 22 shows the results of the initial polar computations. All configurations show very similar lift predictions in the linear part of the lift curve, each without variations in lift over the last cycles per angle of attack. In the non-linear part and near maximum lift however, the predictions differ in terms of maximum lift itself as well as in the associated angle of attack. The deviations from a mean value still lie within the desired prediction accuracy and don't exceed values of $\Delta C_{L,max} < 0.07$ for maximum lift and $\Delta \alpha_{max} < 0.5^\circ$ for the associated angles of attack.

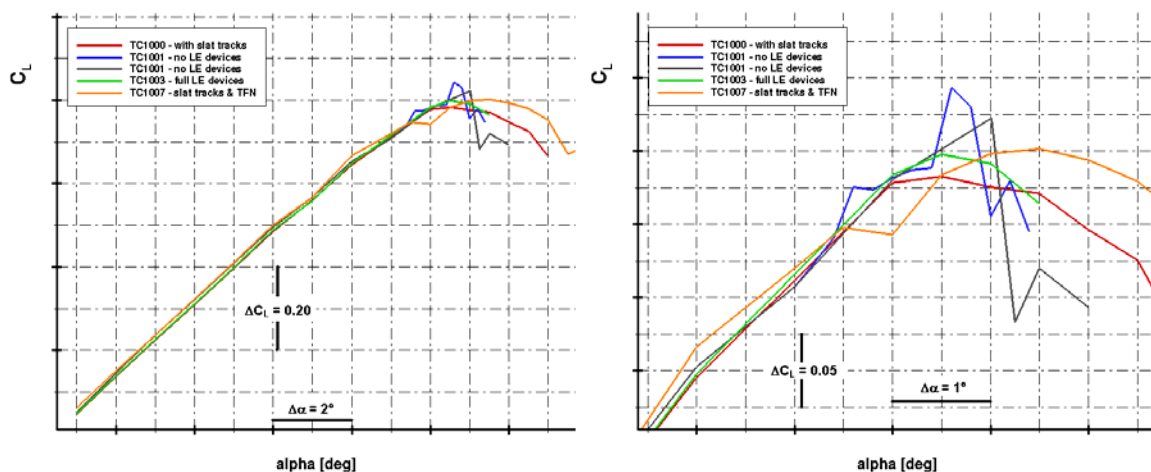


Figure 22. Initial polar computations for TC 1000, TC 1001, TC 1003 and TC 1007

A comparison between TC 1001 without any leading edge devices (grey), TC 1000 with slat tracks (red) and TC 1003 with slat tracks and de-icing pipe (green) shows as expected an earlier but significant less abrupt stall.

Since it is known from other investigations¹⁶ that the solutions near maximum lift may well be dependent on the initial conditions and therefore the size of increments in angle of attack, for TC 1001 the last 1.5 degrees of the lift curve were simulated again with smaller increments of $\Delta\alpha = 0.2^\circ$. The results (blue) show a gain in maximum lift of 2 lcts at a 0.4° lesser angle of attack over the initial simulations (grey). This as well as the local increase in lift 1° below α_{\max} indicate either the necessity of very small changes in angle of attack near maximum lift or the need to apply time resolved uRANS simulations for the upper part of the lift curve. Both are being investigated at the moment.

In addition to these findings TC 1003 (green) exceeds TC 1000 (red) in maximum lift by 1.6 lift counts (lcts) against the expected trend while the lift oscillations over the last two periods in convergence history add up to 4.3 lcts. Since the lift predictions are quite similar for the linear part a major grid dependency seems unlikely but is possible nonetheless. So far also for this case analysis is still ongoing and no final assessment is possible.

2. Stall Patterns and Vortices

Although maximum lift and α_{\max} differ for the investigated configurations, the stall patterns are very similar. Figure 23 shows them exemplarily based on the pressure distributions and skin frictions lines for TC 1007 with the TFN for six different angles of attack on the lift curve.

At low angles of attack and within the linear part of the lift curve (top left, top right) the flow on the flap is separated over a wide spanwise extension while the flow on the main wing is mostly attached. Near the wingtip however, comparatively small areas of detached flow can be observed. With increasing angle of attack (middle left) and in the non-linear part of the lift curve (middle right) the flow on the flap behind the nacelle is more and more attached which leads to an overall increase in lift, even if the flow on the outer parts of the wing is detached. Also an increased loading and possible separations on the inboard part of the inboard flap can be seen.

At the wing pylon intersection areas of high aerodynamic loading can be observed which impose a possible cause for stall at even higher angles of attack. However, this is supposed to be avoided by the placement of the inboard nacelle strake.

The lower left and lower right picture in Figure 23 show pressure distributions and skin frictions lines at maximum lift and post-stall, respectively. One can see that breakdown in lift occurs gradually behind the nacelle due to separations at the wing trailing edge, even though the flow at the inboard wing trailing edge is weakened as well. Since experience from other investigations³ and literature³² would suggest a breakdown in lift possibly starting at the inboard wing trailing edge near the fuselage if an inboard nacelle strake is mounted on the engine, this corroborates the assumption that the nacelle strake might not be fully operational in the CAD representation.

Then again Figure 24 shows exemplarily for TC 1001 a very good resolution of the different vortices over a wide range of angles of attack even at post-stall conditions which does not favour the assumption of an insufficient grid resolution. In fact for angles of attack in the non-linear part of the lift curve (middle right) a counter-clockwise rotating vortex emerging near the inboard slat's outboard edge is visible which was also visible for the stage 2 case without nacelle strake in EUROLIFT II³³. For stage 3 configurations with nacelle strake however this vortex got significantly decreased in strength leading to a strengthened flow behind the nacelle and delayed stall.

Therefore the effectiveness of the strake seems questionable to some degree in the simulations and since even small deviations in placement, i.e. CAD preparation, may alter the strake vortex' position in space and so may cause a significant impact on the flow physics, a comparison between the strake mounted on the ATRA and the CAD representation is scheduled to take place in early 2012.

Another possibility for the predicted stall mechanism caused by a growing trailing edge separation on the main wing behind the nacelle however could indeed be a very well balanced loading of the inboard wing. Comprehensive verification studies with flight test data will address this topic, even if the still ongoing verification studies should point to a not properly placed or to a certain degree ineffective strake.

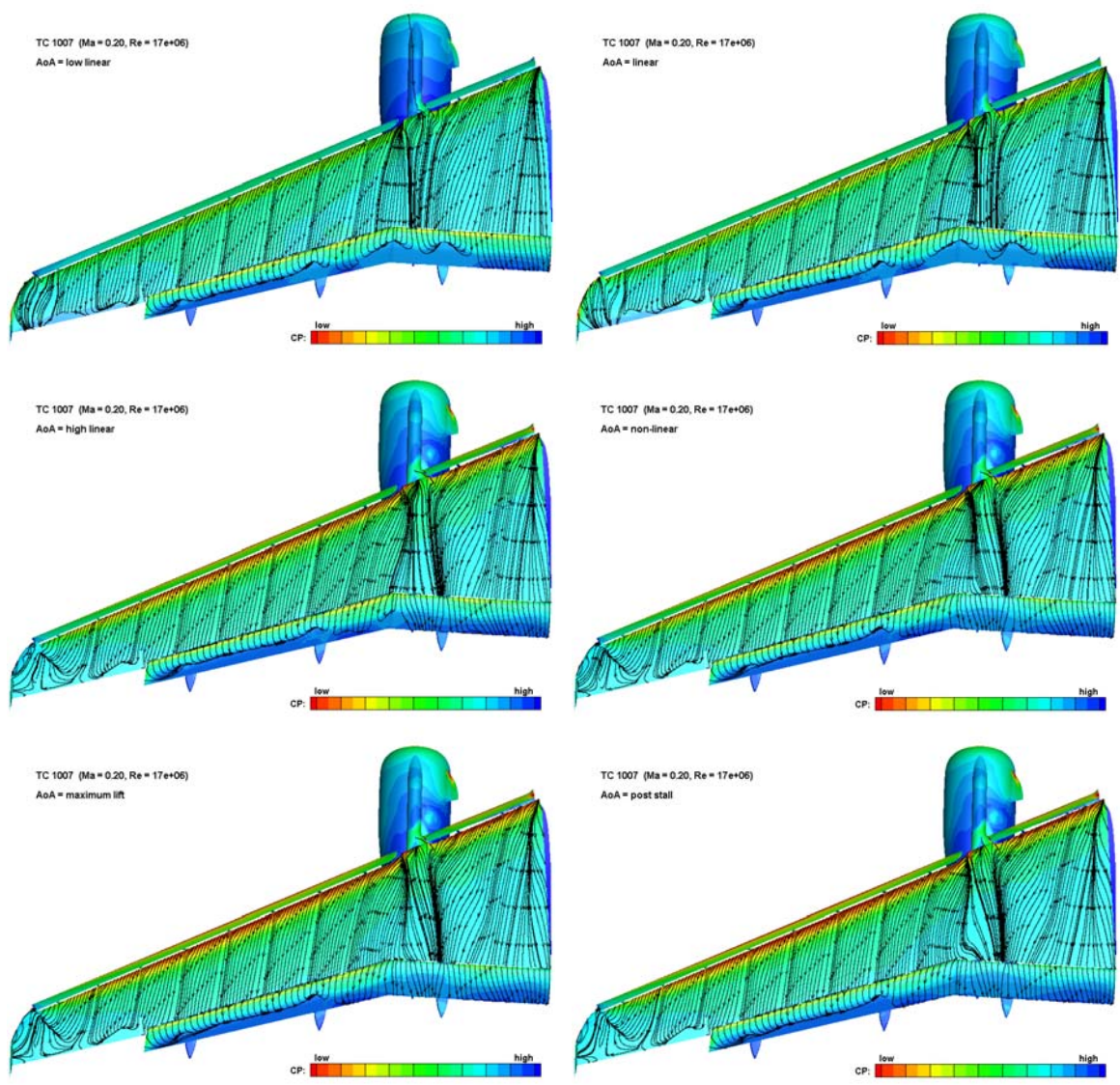


Figure 23. TC1007: Pressure distributions and skin friction lines

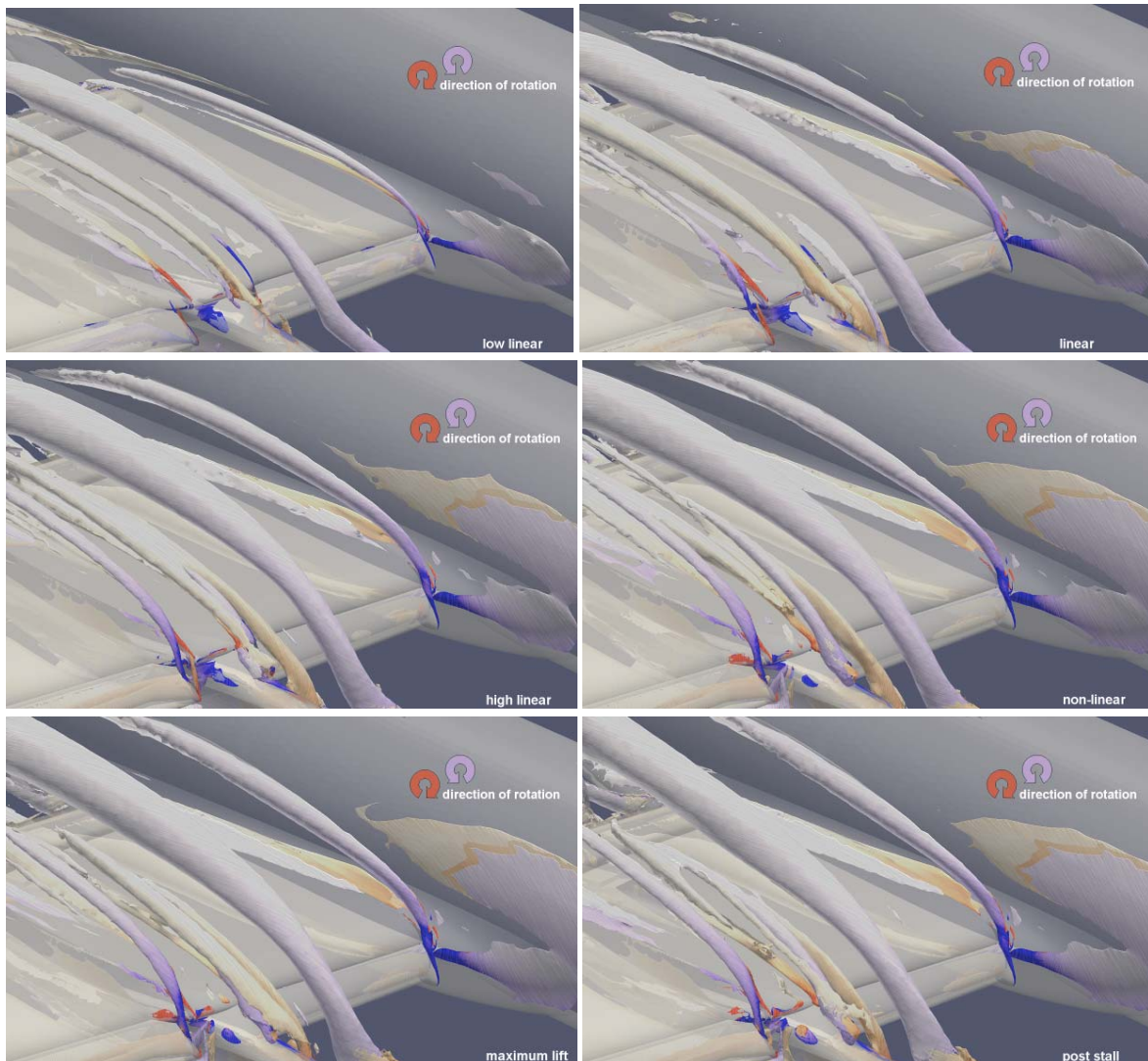


Figure 24. TC1001: Vortex systems of TC 1001

3. Influence of the operational engine

One of the main differences between flight test and wind tunnel tests is the engine, which produces in flight tests even at approach settings a minimum of thrust, whereas usually in wind tunnel tests through-flow nacelles are used which on top have very often an increased exhaust area to match the flight conditions mass flow. Especially for the landing configuration with the fully deployed flap this is a source of uncertainty in maximum lift prediction. A comparison of the pressure distributions on the wing and the flap in the wake of the nacelle is given in Figure 25 for TC 1001 with the operational engine and TC 1007 with the TFN.

For low angles of attack (top) only minor differences can be seen on the wing (top left), whereas on the flap (top right) the jet causes a shift of the stagnation point to the pressure side and as a consequence an even larger separation on the suction side (black line).

For higher angles of attack in the non-linear part of the lift curve (middle) the circulation on the flap decreases in the wake of the engine (middle right, black curve) and for TC 1007 with the TFN with increased exhaust diameter circulation decreases even more (middle right, red curve). As a consequence on the main wing the pressure near the trailing edge raises more (middle left, red curve) resulting in an additional comparative loss in lift.

At the same angles of attack near maximum lift the operational engine's jet causes an increased circulation on the flap (bottom right, black curve) and as a consequence leads to a significantly larger separation on the main wing (bottom left, black curve) causing stall.

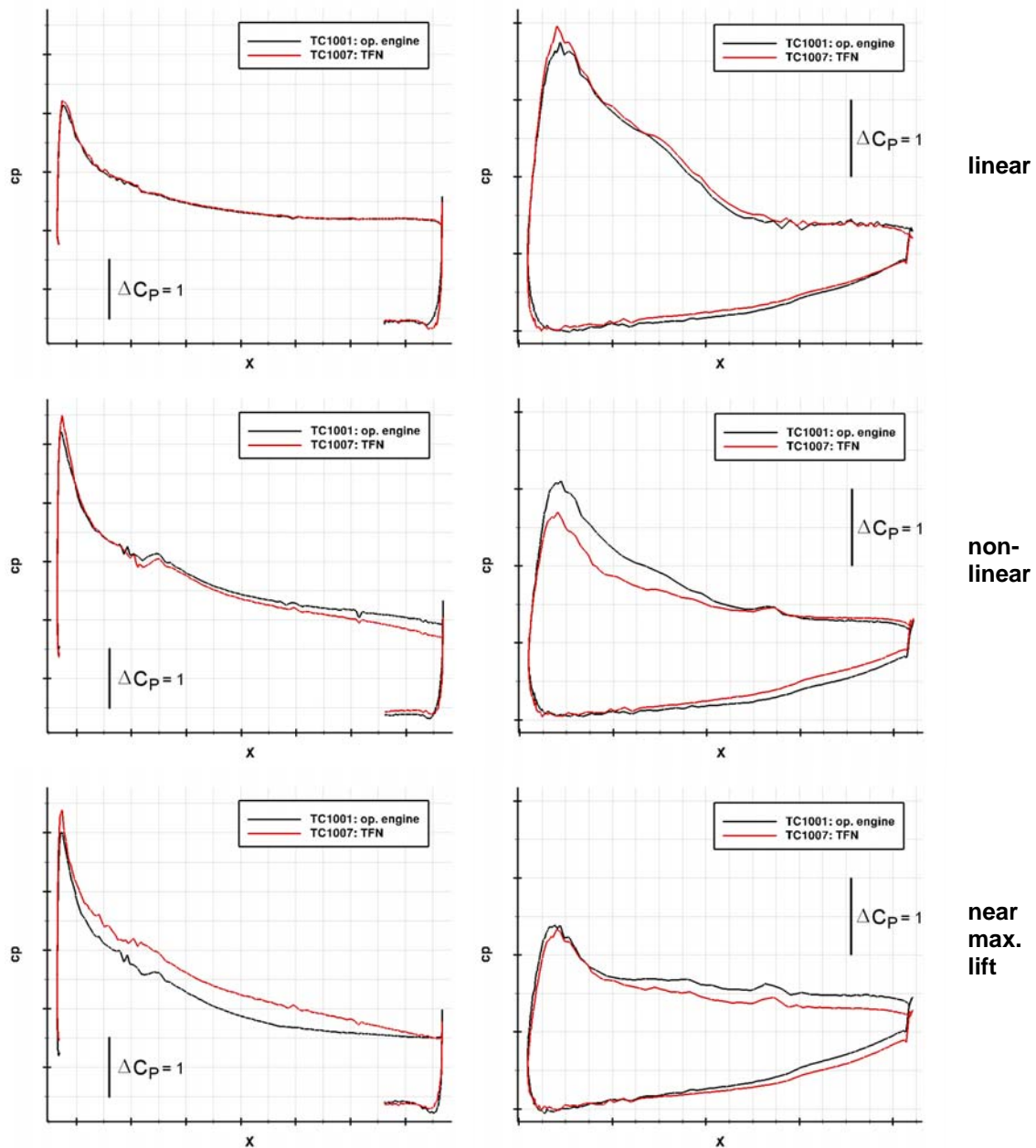


Figure 25. Influence of the operational engine on the pressure distribution in the wake of the nacelle

V. Conclusion

In this paper we presented the structure of the task “Numerical Simulations” of the project “HINVA - High Lift INflight Validation”, in which flight tests with DLR’s A320-232 “ATRA” in landing configuration will be carried out. The CAD model for the numerical simulations is very precise and the numerical grids that were generated resolve very well the assumable important flow phenomena dominating maximum lift. First results show that only small increments in angle of attack can be applied and that in the non-linear part of the lift curve time resolved uRANS simulations might be necessary to predict maximum lift within the desired accuracy. Numerically predicted stall patterns and vortex systems, which are very well resolved, indicate that the size and the position of the nacelle strake in the CAD model should be checked before conducting further simulations. However, the variations in maximum lift and the associated angle of attack lie within the desired prediction accuracy.

Acknowledgments

The authors like to acknowledge the Federal Ministry of Economics and Technology for funding this research activity. Special thanks to all involved HINVA partners for their engagement and the technical contributions.

References

- ¹ Rudolph, P.K.C.: "High-Lift Systems on Commercial Subsonic Airliners". NASA CR 4746, 1996.
- ² Smith, A.M.O.: "High-Lift Aerodynamics," AIAA 6th Aircraft Design, Flight Test and Operations Meeting, Paper 74-939, 1974
- ³ v.Geyr, H. and Schade, N.: "CFD Prediction of Maximum Lift Effects on Realistic High-Lift-Commercial-Aircraft-Configurations within the European project EUROLIFT II". 25th AIAA Applied Aerodynamics Conference, Paper 2007-4299, 2007.
- ⁴ Rudnik, R.: "HINVA - High lift INflight VALidation". 50th AIAA Aerospace Sciences Meeting, (submitted for publication), 2012.
- ⁵ Dassault Systemes: "CATIA V5 R18", www.3ds.com/products/catia.
- ⁶ Intl. TechneGroup Inc.: "CADFix", www.transcendata.com/products/cadfix.
- ⁷ Rudnik, R. and Ronzheimer, A.: "Numerical Investigation of the Flow around different Slat Tracks of a Swept HighLift Wing Segment," Notes on Numerical Fluid Mechanics and Multidisciplinary Design, Vol. 87, 2002, pp. 58–65.
- ⁸ Keller, D.: Numerical Investigation of Vortex and Separation Behavior on a Future Civil Transport Aircraft in High-Lift Configuration", Diploma Thesis, RWTH Aachen, 2010.
- ⁹ CentaurSoft, "CENTAUR Software". <http://www.centaursoft.com>, retrieved May 2011.
- ¹⁰ Acheson, K. and Kornegay, B. and Lau, H.-F.: "Influence and Control of Unstructured Volume Meshes for Enhanced Fidelity Performance Predictions". AIAA paper 2011-3984, 2011.
- ¹¹ Munday, S. and Martineau, D. and Verhoeven, N.: "Automated Hybrid Mesh Generation for Industrial High-Lift Applications". AIAA paper 2007-268, 2007.
- ¹² Crippa, S.: "Improvement of Unstructured Computational Fluid Dynamics Simulations Through Novel Mesh Generation Methodologies". Journal of Aircraft, Vol. 48, No. 3, 2011, pp. 1036-1044.
- ¹³ Pointwise: "Gridgen". <http://www.pointwise.com/gridgen>
- ¹⁴ Schwamborn, D., Gerhold, T., Heinrich, R.: "The DLR TAU-Code: Recent Applications in Research and Industry". In Wesseling, P., Onate, E., Periaux, J. (Eds.): "Proceedings of the European Conference on Computational Fluid Dynamics". ECCOMAS, 2006.
- ¹⁵ Gerhold, T.: "Overview of the Hybrid RANS Code TAU". In "MEGAFLOW - Numerical Flow Simulation for Aircraft Design", Notes on Numerical Fluid Mechanics and Multidisciplinary Design", Vol. 89, Heidelberg, 2005, pp. 81-92.
- ¹⁶ Crippa, S. and Melber-Wilkending, S. and Rudnik, R.: "DLR Contribution to the First High Lift Prediction Workshop". AIAA paper 2011-938, 2011.
- ¹⁷ Rumsey, C. et al.: "Summary of the First AIAA CFD High-Lift Prediction Workshop". Journal of Aircraft, Vol. 48, No. 6, 2011, pp. 2068-2079.
- ¹⁸ Spalart, P. and Allmaras, S.: "A One-Equation Turbulence Model for Aerodynamic Flows," AIAA paper 1992-439, 1992
- ¹⁹ Eisfeld, B.: "Numerical Simulation of Aerodynamic Problems with the SSG/LRR- ω Reynolds Stress Turbulence Model Using the Unstructured TAU Code". In: New Results in Numerical and Experimental Fluid Mechanics VI, Vol. 96 of Notes on Numerical Fluid Mechanics and Multidisciplinary Design, Springer, 2007, pp. 356-363.
- ²⁰ Krumbein, A. and Krimmelbein, N. and Schrauf, G.: "Automatic Transition Prediction in a Hybrid Flow Solver—Part 1: Methodology and Sensitivities". Journal of Aircraft, Vol. 46, No. 4, 2009, pp. 1176–1190.
- ²¹ Schrauf, G.: "COCO: A Program to Compute Velocity and Temperature Profiles for Local and Nonlocal Stability Analysis of Compressible, Conical Boundary Layers with Suction" ZARM, Center of Applied Space Technology and Microgravity, 1998.
- ²² Schrauf, G.: "LILO 2.1. User's Guide and Tutorial" Tech. rep., 2006, GSSC Technical Report 6, originally issued Sep. 2004, modified for Version 2.1.
- ²³ Krimmelbein, N. and Krumbein, A.: "Automatic Transition Prediction for Three-Dimensional Configurations with Focus on Industrial Application". AIAA Journal of Aircraft, Vol. 48, No. 6, 2011, pp. 1878-1887.
- ²⁴ Greff, E.: "In-Flight Measurement of Static Pressures and Boundary-Layer State with Integrated Sensors". AIAA Journal of Aircraft, Vol. 28, No. 5, 1991, pp. 289-299.
- ²⁵ Wermes, M.: "Konstruktion und Aufbau einer verfahrenbaren Grenzschichtsonde für Flugmessungen". Proceedings 60th DLRK, Paper No. DLRK2011-241476, Bremen, Germany, 2011.
- ²⁶ Melber-Wilkending, S. and Wichmann, G.: "Application of Advanced CFD Tools for High Reynolds Number Testing". AIAA Paper 2009-0418, 2009.
- ²⁷ Melber-Wilkending, S. and Heidebrecht, A. and Wichmann, G.: "CFD Validation by Wind Tunnel Measurements: Uncertainty Assessment by Numerical Simulation of Complete Wind Tunnel Flows". NATO-RTO, AVT 147, 2007.
- ²⁸ Schütte, A. et al.: "Numerical Simulation of Maneuvering Aircraft by Aerodynamic, Flight Mechanics and Structural Mechanics Coupling". AIAA Paper 2007-1070, 2007.
- ²⁹ MSC Software Corporation: "NASTRAN". http://www.mssoftware.com/products/msc_nastran.cfm.
- ³⁰ Keye, S.: "Fluid-Structure Coupled Analysis of a Transport Aircraft and Flight-Test Validation". Journal of Aircraft, Vol. 48, No. 2, 2011, pp. 381-390.
- ³¹ Heinrich, R. and Wild, J. and Streit, T. and Nagel, B.: "Steady Fluid-Structure Coupling for Transport Aircraft", 7th ONERA-DLR Aerospace Symposium, ODAS 2006, Toulouse, France, 4th-6th October 2006.
- ³² Haines, A.: "Scale Effects at High Lift and Low Speeds". In :Young, A. (Ed.): "Scale Effects on aircraft and Weapon Aerodynamics", AGARD-AG 323, 1999, pp. 27-65
- ³³ v.Geyr, H. and Schade, N.: "Numerical Investigations of a Realistic High Lift Configuration". EUROLIFT II Technical Report No. D2.1.3-8. Braunschweig, Germany, 2007 (unpublished).